Intermetallics 120 (2020) 106741

Contents lists available at ScienceDirect

Intermetallics

journal homepage: http://www.elsevier.com/locate/intermet

Effects of temperature and strain rate on plastic deformation mechanisms of nanocrystalline high-entropy alloys

Li Li [a], Haotian Chen [a], Qihong Fang [a], Jia Li [a,*], Feng Liu [b], Yong Liu [b], Peter K. Liaw [c]

[a] *State Key Laboratory of Advanced Design and Manufacturing for Vehicle Body, Hunan University, Changsha, 410082, PR China*
[b] *State Key Laboratory of Powder Metallurgy, Central South University, Changsha, 410083, PR China*
[c] *Department of Materials Science and Engineering, The University of Tennessee, Knoxville, TN, 37996, USA*

ARTICLE INFO

Keywords:
High entropy alloy
Molecular dynamics simulation
Temperature
Strain rate
Diffusion coefficient
Plastic deformation

ABSTRACT

The nanocrystalline high-entropy alloys (HEAs) can be regarded as ideal substitution materials for use in aero engines due to their outstanding mechanical properties. Owing to the crucial importance on the evaluation of mechanical properties in nanocrystalline HEAs, the identification of the plastic deformation mechanism remains a challenging topic. Considering the fact that nanocrystalline HEAs suffer from the high-temperature service, the roles of strain rate and temperature on their deformation characteristics should be examined. Here, we report the impact of strain rate and temperature on the mechanical properties and deformation behaviors of nanocrystalline HEAs. This issue was investigated by a series of molecular-dynamics tensile tests at different strain rates ranging from 5×10^7 to 1×10^{10} s^{-1} and temperatures ranging from 10 to 1,200 K. The results show that the dislocation slip controls the preferred deformation mechanism at low temperatures and high strain rates. When the temperature rises and strain rate reduces, grain-boundary sliding dominates the primary deformation mechanism at elevated temperatures. Moreover, the occurrence of the face-centered-cubic (fcc) to body-centered-cubic (bcc) phase transformation can effectively enhance the plasticity of HEAs. The synergistically-integrated experimental and modeling efforts at the nanoscale will help understand, control, and optimize the mechanical behaviors of nanocrystalline HEA systems, thereby enabling the development of advanced nanocrystalline HEAs.

1. Introduction

High-entropy alloys (HEAs) with multi-component equal or nearly equal elements exhibit many excellent properties [1–5], due to their severe lattice distortion and sluggish diffusion effects [6–12]. For example, a single face-centered cubic (fcc) FeCrCoNiMn HEA has exceptional damage tolerance and fracture toughness, compared to most alloys [13–15]. The transmission electron microscopy reveals that the deformation mechanism changes from the conventional dislocation glide at room temperature to nano-twinning at a low temperature of 77 K [15,16].

Recently, the bulk nanocrystalline $Co_{25}Ni_{25}Fe_{25}Al_{7.5}Cu_{17.5}$ HEA has been produced by mechanical alloying combined with consolidation via spark plasma sintering [17]. This HEA shows a high yield strength dramatically larger than those of most previously-reported fcc-structured HEAs, such as FeCrCoNiMn. Although the deformation behaviour and strengthening mechanism of bulk nanocrystalline HEAs have been revealed at room temperature, this issue in HEAs at high temperatures is still not understood [12–14]. Hence, the nanocrystalline $Co_{25}Ni_{25}Fe_{25}Al_{7.5}Cu_{17.5}$ HEA would be chosen as the research object in this investigation. However, the deformation mechanism of HEAs in a wide high temperature range has rarely been studied.

Molecular dynamics (MD) simulations are a powerful tool to study the relationship between microstructure and properties at the nanoscale. Many researches have employed MD simulation to investigate the deformation mechanism in HEAs [18–27]. However, the interatomic potential of HEA do not consider any information, such as the electron density distribution and magnetic effect, and a limitation of these conventional interatomic potentials cannot solve the problem of heat transfer and magnetic field. For instance, the mechanical behaviors and deformation mechanisms of AlCrCuFeNi under the scratched condition and the tensile deformation were investigated by MD simulation [18, 19]. The results indicate that the dislocation gliding, and dislocation pinning due to the severe lattice-distortion and the solute atoms are the main plastic deformation mechanisms. Moreover, MD simulation were employed to investigate the tensile and compressive behaviors of

---

[*] Corresponding author.
E-mail address: lijia123@hnu.edu.cn (J. Li).

https://doi.org/10.1016/j.intermet.2020.106741
Received 22 December 2019; Received in revised form 30 January 2020; Accepted 6 February 2020

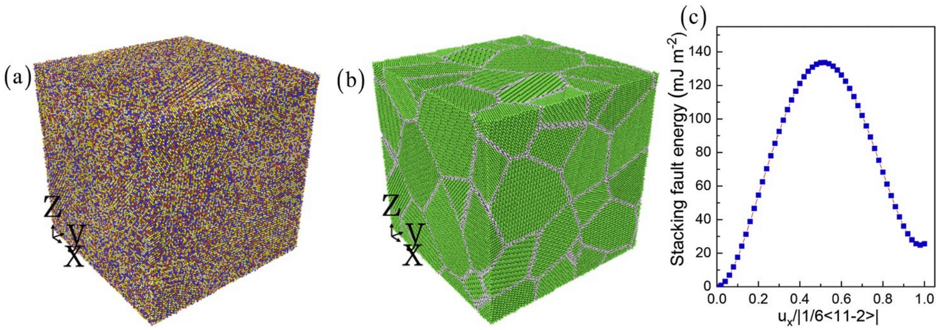

Fig. 1. Schematic model of the nanocrystalline HEA $Co_{25}Ni_{25}Fe_{25}Al_{7.5}Cu_{17.5}$ using MD simulations. ● Cu, ● Ni, ● Fe, ● Al, and ● Fe. The atoms are colored according to the element type (a), and the CNA value (b). Stacking fault energy vs. displacement (c).

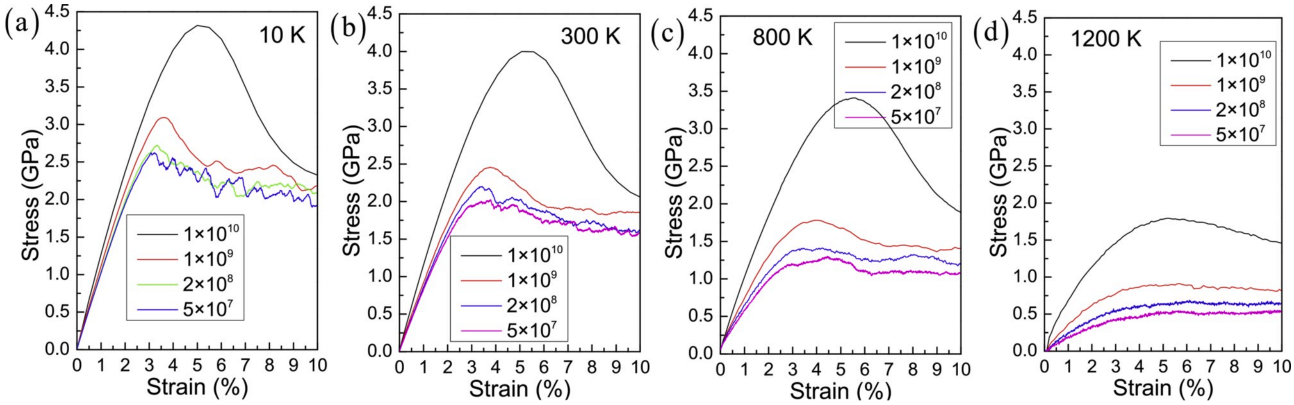

Fig. 2. Stress-strain relationship for different temperatures and strain rates in the $Co_{25}Ni_{25}Fe_{25}Al_{7.5}Cu_{17.5}$ HEA.

$Al_xCrCoFeCuNi$ HEAs, the effects of element concentration on the mechanical and physical behaviors have been discussed [20,21]. By controlling cooling rates to obtain the structural hierarchy, the mechanical behavior of AlCoCrCuFeNi HEA is optimized to maximize its high strength [22]. The structure and migration behavior of symmetrical tilt grain boundary (GB) in CuNiCoFe HEA is studied, and solute segregation suppresses GB migration for reduced grain growth [23]. Recently, metastability design for HEAs has attracted wide attention, many researches have explore the TRIP and TWIP in HEAs based on the MD simulation [24–27].

In the present work, we investigated the effects of temperature and strain rate on the deformation mechanism of nanocrystalline HEAs. After a description of the technical details of MD simulations, we firstly addressed the effects of temperature and strain rate on mechanical properties. We then investigated the influences of temperature and strain rate on the deformation behaviors, and finally computed the diffusion coefficient.

2. Simulation details

Using the Voronoi construction method [28,29], the cubic nanocrystalline HEA samples containing 27 random-crystallographic -orientation grains were built, as shown in Fig. 1a and b. The sizes of the nanocrystalline HEA sample are 30 × 30 × 30 nm^3. The nanocrystalline HEA has 2,295,393 atoms, and its average grain size is 12 nm. Using the LAMMPS, MD simulations are carried out [30]. All dimensions are applied to periodic boundary conditions. The various temperatures used are 10 K, 300 K, 800 K, and 1,200 K. For each temperature, the nanocrystalline HEA sample is relaxed for 100 ps by the Nose'-Hoover isobaric-isothermal (NPT) ensemble. The embedded atom method (EAM) potential is used to study the deformation behaviour [26,31]. The nanocrystalline HEA deforms to the strain of 10% along the *x* direction at the different strain rates ranging from 5×10^7 s^{-1} to 1×10^{10} s^{-1} during the tensile loading. By the Ovito software [32], the evolution of the local atomic structure was distinguished via the common-neighbor analysis (CNA) [33], where the green color stands for the fcc structure, the red color denotes the hexagonal close-packed (hcp) structure, and the white color represents other structures, including dislocations and GB. The deformation mechanism of nanocrystalline metal depends on the stacking fault energy (SFE), which determines deformation twinning or dislocation glide. Hence, the curve of SFE in HEA is presented in Fig. 1c. Here, SFE of HEA is 25.5 mJ m^{-2} in accordance with the previous work [26,34,35], leading to that the partial dislocations are more likely to occur, compared to the full dislocation.

3. Results and discussions

3.1. Mechanical properties

The elastic constants of C_{11}, C_{12}, and C_{44} were obtained by the current embedded atom method (EAM) potential in the fcc HEA, and the corresponding values are 147.6, 108.5, and 84.6 GPa, respectively. The elastic constants of the fcc $Co_{25}Ni_{25}Fe_{25}Al_{7.5}Cu_{17.5}$ HEA complied with the generalized elastic-stability criteria of the cubic crystal at the hydrostatic pressure [36], namely, $(C_{11}–C_{12}) > 0$, $C_{11} > 0$, $C_{44} > 0$, and $(C_{11} + 2C_{12}) > 0$. According to the current work [37], the Young's modulus, E, shear modulus, G, and bulk modulus, B, are 151.4, 58.6, and 121.5 GPa, respectively.

As well known, due to the short-time duration, MD simulations always involve extremely-high strain rates (of typically larger than 10^7 s^{-1}), much higher than in the conventional tensile/compressive experiments. Compared with the results from experiments, MD simulations

Table 1
The fitting parameters of ultimate strengths at different temperatures.

Parameters Temperatures	10 K	300 K	800 K	1200 K
a	2.598	1.968	1.207	0.433
b	1.091×10^{-7}	1.936×10^{-6}	3.448×10^{-6}	3.835×10^{-5}
c	0.7198	0.6021	0.5806	0.455

Table 2
The fitting parameters of average flow stresses at different temperatures.

Parameters Temperatures	10 K	300 K	800 K	1200 K
a	2.135	1.657	1.060	0.391
b	2.407×10^{-11}	4.969×10^{-8}	1.623×10^{-6}	5.994×10^{-5}
c	1.07	0.7473	0.6016	0.4324

are more complex because the strain rate has a significant effect on the deformation mechanisms. For example, it is generally agreed that higher strain rates promote the deformation twinning in nanocrystalline materials [38]. Recently, the phase transformation and dislocation evolution in dual-phase FeCoCrNiMn HEAs have been successfully investigated by means of MD simulations [25]. From the perspective of deformation mechanisms, the higher strain rate in the $Co_{25}Ni_{25}Fe_{25}Al_{7.5}Cu_{17.5}$ HEA could greatly lead to the formation of deformation twinning, as compared to the low strain rate. Hence, MD simulations can provide the continuous and intuitive microstructure evolution, thereby shedding light onto the deformation mechanisms of HEAs at atomic-level processes. Here, using MD simulation, the stress-strain response in the nanocrystalline Co25Ni25Fe25Al7.5Cu17.5 HEA is studied based on our previous work [26]. Fig. 2 shows that the ultimate strength and average flow stress in the HEA decline with the increase of temperature, owing to the softening effect at high temperatures. Furthermore, the ultimate strength and average flow stress decline sharply when the strain rate reduces from 1×10^{10} to 1×10^{9} s^{-1}, yet they decline slowly when the strain rate goes down from 1×10^{9} to 5×10^{7} s^{-1} (Fig. 2). According to the previous work related to the strain rate [39], the relationship between the strain rate and average flow stress meets a power-function relationship of $\sigma = a + b\dot{\varepsilon}^{c}$, where σ is the average flow stress, $\dot{\varepsilon}$ is the strain rate, and *ab*, and *c* are the fitting parameters of the strain-rate sensitivity. Tables 1 and 2 show the fitting parameters of ultimate strengths at different temperatures. The corresponding fitting curves to reveal the temperature and strain rate on the mechanical properties are presented in Fig. 3. Based on the power-function relationship, the values of the average flow stress and ultimate strength in a quasistatic state ($\dot{\varepsilon} \rightarrow 0$) can be obtained. The average flow stress and ultimate strength in a quasistatic state are equal to the fitting parameter *a*. Hence, the ultimate strength of 1.968 GPa from current MD simulation at room temperature is consistent with that of 1.936 GPa from the previous experiment [17].

In view of the previous research [40–43], a mechanism-based constitutive model coupling the lattice distortion-dependent solid-solution strengthening is proposed to investigate the mechanical behaviors of the nanocrystalline HEAs. The flow stress of HEAs can be expressed as

$$\sigma_{flow} = \sigma_0 + M\alpha\mu b\sqrt{\rho} + \sigma_{GB} + \sigma_{ss} + \sigma_b \tag{1}$$

where the first term σ_0 on the right-hand side of the equation stands for the lattice-friction stress, the second term $M\alpha\mu b\sqrt{\rho}$ represents the dislocation strengthening, the third term σ_{GB} is GB strengthening, the fourth term σ_{ss} denotes the lattice-distortion-dependent solid-solution strengthening, and the last term σ_b represents the back stress. The expression of the lattice-distortion-dependent solid-solution strengthening introduced by a single element in HEAs can be expressed as [44,45].

$$\sigma_f^i = A\mu c_i^{2/3}\delta_i^{4/3} \tag{2}$$

The $Co_{25}Ni_{25}Fe_{25}Al_{7.5}Cu_{17.5}$ HEA is assumed as a pseudo-binary solid solution based on the previous study [44,46], due to extremely-close atomic radii and shear moduli among Co, Ni and Fe elements, and significantly-larger atomic radii, and markedly-smaller shear moduli for Al and Cu, compared to the Co, Ni, and Fe elements. Therefore, the Al and Cu elements are regarded as solute elements in solvents composed of Co, Ni and Fe elements. A detailed description of the lattice-distortion-dependent solid-solution strengthening and the other strengthening mechanism in Eq. (1) is given in Appendix A. Fig. 4

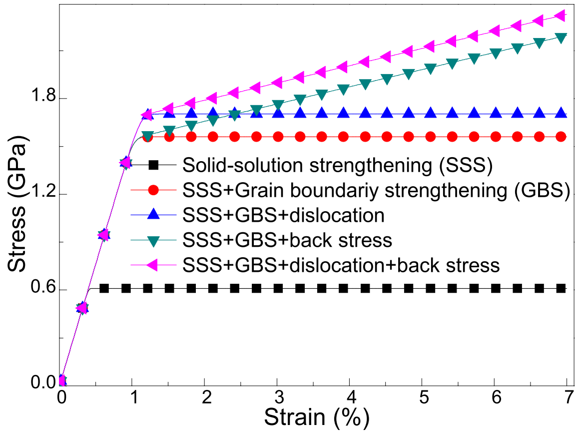

Fig. 4. The contributions from various strengthening mechanisms in nanocrystalline $Co_{25}Ni_{25}Fe_{25}Al_{7.5}Cu_{17.5}$ HEAs under uniaxial tensile deformation.

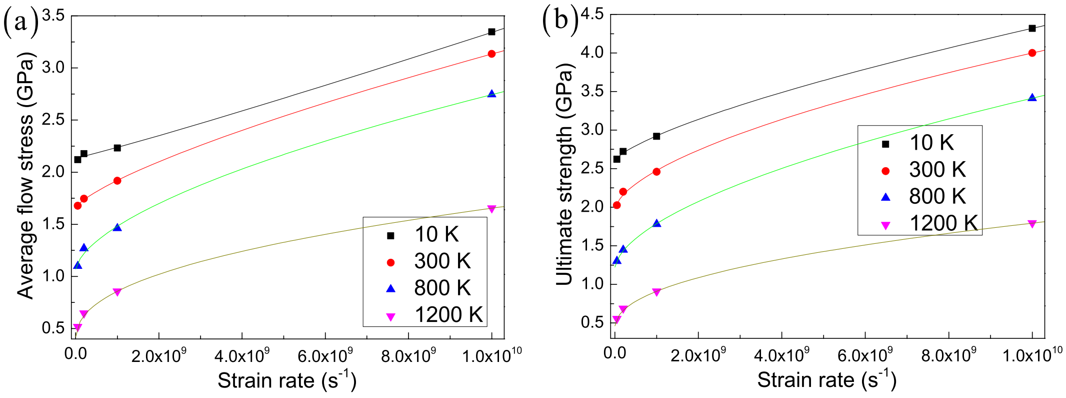

Fig. 3. Variations of the average flow stress and strain rate (a), variations of the ultimate strength and strain rate (b), and the corresponding fitting curves.

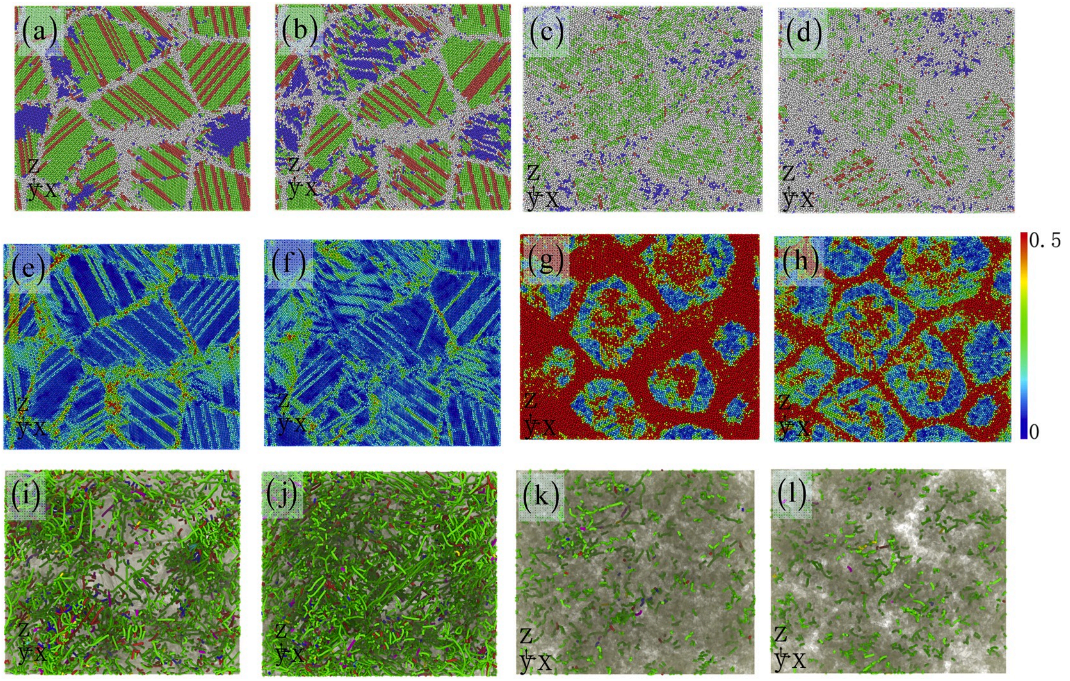

Fig. 5. GB structure after tension deformation at different temperatures and strain rates: 10 K and 5 × 10^7 s^{-1} (a), 10 K and 1 × 10^{10} s^{-1} (b), 1,200 K and 5 × 10^7 s^{-1} (c), and 1,200 K and 1 × 10^{10} s^{-1} (d). Atomic shear-strain distribution after tension deformation at different temperatures and strain rates: 10 K and 5 × 10^7 s^{-1} (e), 10 K and 1 × 10^{10} s^{-1} (f), 1,200 K and 5 × 10^7 s^{-1} (g), and 1,200 K and 1 × 10^{10} s^{-1} (h). Dislocation evolution at different temperatures and strain rates: 10 K and 5 × 10^7 s^{-1} (i), 10 K and 1 × 10^{10} s^{-1} (j), 1,200 K and 5 × 10^7 s^{-1} (k), and 1,200 K and 1 × 10^{10} s^{-1} (l). In (i–l), as indicated by the line colors, dislocations, including perfect dislocations (— blue line), Shockley partials (— green line), Hirth (— light-yellow), and stair-rod (— pink line) dislocations, have nonstandard Burgers vectors in the fcc phase.

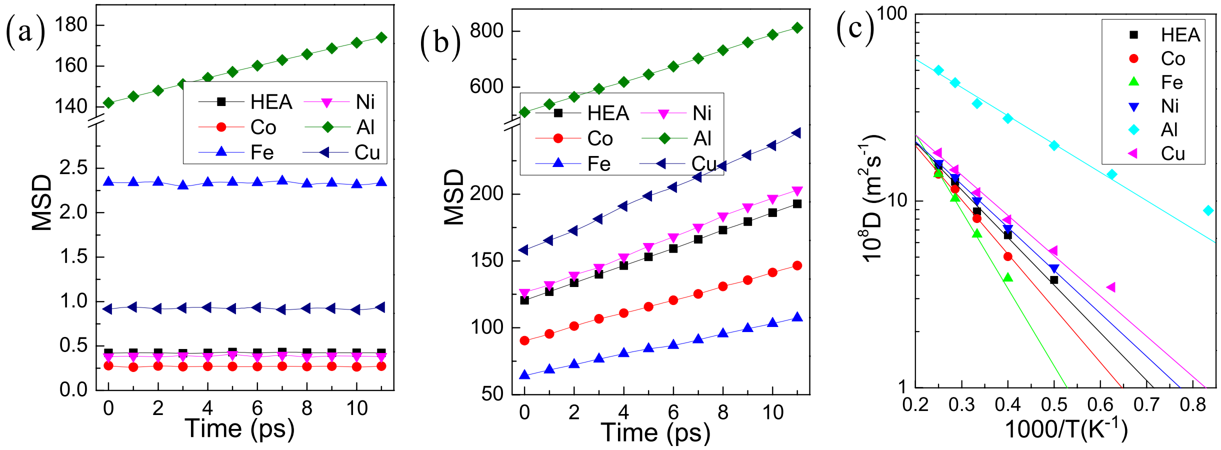

Fig. 6. MSD in the HEA, Ni, Co, Fe, Al, and Cu at the temperatures of 1,200 K (a) and 2,500 K (b). Relationship between the diffusion coefficient and temperature in the HEA, Ni, Co, Fe, Al, and Cu (c).

shows that the various strengthening mechanisms contributed to the flow stress in nanocrystalline $Co_{25}Ni_{25}Fe_{25}Al_{7.5}Cu_{17.5}$ HEAs at room temperature. The yield strength is largely derived from the solid-solution strengthening and GB strengthening, while the strain hardening is mainly contributed from the back stress strengthening and the dislocation strengthening. Thereinto, GB strengthening is significantly greater than solid-solution strengthening in the increase of yield stress. The back stress makes the most contribution to the strain hardening with the continuously increasing plastic strain, whereas the dislocation evolution in the grain interior only provides strain hardening at the initial stage of plastic deformation owing to the consideration of the additional dislocation dynamic recovery at GBs.

3.2. *Deformation behaviour*

In order to understand the effects of the strain rate and temperature on the deformation mechanism, the atomic microstructure and shear-strain curve of the nanocrystalline HEA subjected to the tension deformation are performed [33,47]. The microstructure, including dislocations and GBs, in the deformed nanocrystalline HEA at temperatures of 10 and 1,200 K after the tensile strain of 10% are presented in Fig. 5a–d and Fig. 5i-l. The region of the local high shear strain is generated along GBs of the nanocrystalline HEA, as shown in Fig. 5e–h. The plastic deformation is dominated by two mechanisms, such as, dislocation glide and GB sliding, as observed in Fig. 5. For the HEA sample at low temperatures and low strain rates, a large number of dislocations are

Table 3
Material parameters used in the present model for the nanocrystalline HEA.

Parameter	Symbol	Magnitude
Elastic modulus (GPa)	E	151.4
Shear modulus (GPa)	μ	58.6
Poisson's ratio	A	0.292
Magnitude of the Burger vector (nm)	b	0.256
Empirical constant	B	0.33
Taylor factor	M	3.06
Maximum number of dislocation	N_B	10
Dynamic recovery constant	k_{20}	21.6
Proportionality factor	B	0.025
Mean spacing between slip bands (nm)	ζ	1
Dynamic recovery constant	m	21.5
Reference strain rate (s^{-1})	C	1
Reference grain size (nm)	d_e	580

activated in Fig. 5a and b. Correspondingly, the dislocation density goes from high to low as: 1.61×10^{17} m^{-2} for the temperature of 10 K and strain rate of 1×10^{10} s^{-1}, 8.32×10^{16} m^{-2} for the temperature of 10 K and strain rate of 5×10^7 s^{-1}, 1.11×10^{16} m^{-2} for the temperature of 1,200 K and strain rate of 1×10^{10} s^{-1}, and 1.06×10^{16} m^{-2} for the temperature of 1,200 K and strain rate of 5×10^7 s^{-1} in turn. Moreover, the intragranular shear bands generated by the dislocation interaction occur in only a few grains, while the local high strain region is mainly located in the vicinity of GBs in the other grains. Because of no initial dislocation source inside the grains, the dislocations mainly nucleate from the GBs. The trace of the straight dislocation motion suggests that simple and limited slip systems are activated in the HEA under low temperatures and low strain rates, due to the absence of the cross-slip inhibited by the limited slip systems [47–52]. Hence, the limited dislocation glide can be activated in a small fraction of grains with large Schmid factors. Therefore, the plasticity capability of the HEA sample would reduce at large deformation where the cross-slip inhibited by the large separation between the partial dislocations in HEA with low SFE cannot occur in a small fraction of grains [3,26,52]. Interestingly, the fcc to body-centered-cubic (bcc) phase transformation can be activated (Fig. 5a–d), reducing the local strain, and enhancing the plasticity of the HEA sample, as evidenced from the previous report [26].

For the HEA sample at higher temperatures and strain rates, microstructure and strain during continual plastic deformation are presented in Fig. 5c, d, g, and h. As a result, the high strain region mainly occurs in the vicinity of GB where the thick shear bands are located, as compared to the intragranular shear. This trend suggests that the dislocation nucleation and GB sliding easily take place at high temperatures and strain rates. This phenomenon results from the faster decreasing energy barrier for GB sliding in comparison to that of the dislocation nucleation, leading to the GB-sliding dominated deformation mechanism [53,54]. Moreover, the ultimate strength and average flow stress at the temperature of 1,200 K (or the strain rate of 1×10^{10} s^{-1}) have been reduced by higher than 50%, compared to the ultimate strength and average flow stress at the temperature of 10 K (or the strain rate of 5×10^7 s^{-1}) (Figs. 2 and 3). The current observations agree well with the experimental result [3], where HEA exhibits a good plastic deformation capacity due to atomic-scale lattice distortion to active various deformation mechanisms [3,12,25,26]. The high strain can facilitate the fcc to bcc phase transformation to increase the toughness of HEA, which is also a fact reported in the previous work [6,26].

3.3. *Diffusion coefficient*

The sluggish diffusion plays a critical role in the deformation behavior of HEAs at high temperatures. To reveal the sluggish diffusion, the diffusion coefficient of HEAs should be studied and used to estimate the diffusion difference between pure metals and HEA at elevated temperature. Here, the mobility of atoms can be computed by the mean-square displacement (MSD), $g(t)$

$$g(t) = \langle (r_i(t) - r_i(0))^2 \rangle \tag{3}$$

where $r_i(t)$ and $r_i(0)$ represent the positions of the atom, i, at the times of t and 0, respectively. The bracket "⟨⟩" means the ensemble average, which is computed from averaging over all penetrants and all time origins at t = 0.

The diffusion coefficient, D, is obtained, using the long time limit of MSD by the Einstein relationship

$$D = \frac{1}{6} \lim_{t \to \infty} \frac{\partial g(t)}{\partial t} \tag{4}$$

where t is the elapsed time. The average is carried out over all time origins, and all atoms. The diffusivity corresponds to the slope of the linear MSD versus time, t.

The impurity diffusion coefficient of solids can be described by the Arrhenius equation [55].

$$D = D_0 \exp\left(-\frac{E}{RT}\right) \tag{5}$$

where D_0 stands for the pre-exponential factor, E is the activation energy, T represents the absolute temperature, and $R = 8.314 J\ mol^{-1}\ K^{-1}$ is the gas constant. The parameters of D_0 and E are evaluated from the measurements of diffusion coefficients at a series of temperatures.

The MSD varies as a positive linear relationship over time at 2,000 K, and remains relatively stable over time at 1,200 K (Fig. 6a). The MSD of the HEA is lower than those of Al, Cu, and Fe at the high temperature of 1,200 K. The slopes of the MSD vs. time curve are then used to determine the diffusion coefficients of the HEA, which are found at different temperatures (Fig. 6b). Moreover, the diffusion coefficient in the HEA is relatively low as compared to that of Al, Cu, and Ni, resulting in a slow diffusion effect. The low diffusion coefficient in the HEA can lead to the high stability of the nanocrystalline HEA at high temperatures [3]. The relationship between the reciprocal of the temperature and the logarithm of the diffusion coefficient obeys a good linear dependencies (Fig. 6c), consistent with the Arrhenius behavior. Here, the Arrhenius equation can be expressed by $D = 66.63 \exp(-5869/T)$ in the HEA.

4. Conclusion

In the present work, the mechanical properties, deformation behavior, and diffusion coefficient of nanocrystalline HEA under uniaxial tensile loadings are studied using MD simulations. Considering the critical effects of temperature and strain rate on the microstructural characteristics of the nanocrystalline HEA, its deformation behaviour is explored at the various strain rates ranging from 5×10^7 to 1×10^{10} s^{-1} and temperatures ranging from 1 to 1,200 K. Hence, the underlying mechanism for the plastic deformation is thoroughly investigated via the dynamical microstructural analysis. As the same as the classical alloys, the flow stress and ultimate strength of HEAs are reduced as the temperature increases or the strain rate decreases. The local high shear-strain region mainly occurs along the GB at high temperatures and low strain rates. The plasticity of the nanocrystalline HEA is attributed to the increased GB sliding and dislocation activity, as well as the fcc to bcc phase transformation. At low temperatures and high strain rates, dislocation glide can control the plastic deformation, in place of GB sliding. Conversely, by increasing the temperature or decreasing the strain rate, GB sliding dominates the plastic-deformation behaviour. The synergistically-integrated atomic simulation and dynamical microstructural characteristic at nanoscales will help understand, control, and optimize the mechanical behavior of nanocrystalline HEA systems, thereby enabling the development of advanced nanocrystalline HEAs.

Declaration of competing interest

The authors declare no conflict of interest.

CRediT authorship contribution statement

Li Li: Investigation, Methodology, Validation, Visualization, Writing - original draft, Writing - review & editing. **Haotian Chen:** Investigation, Methodology, Validation. **Qihong Fang:** Funding acquisition, Writing - review & editing, Project administration, Resources, Supervision. **Jia Li:** Conceptualization, Data curation, Formal analysis, Investigation, Methodology, Validation, Visualization, Writing - original draft, Writing - review & editing, Software. **Feng Liu:** Funding acquisition, Writing - review & editing, Resources, Supervision. **Yong Liu:** Funding acquisition, Writing - review & editing, Project administration, Resources, Supervision. **Peter K. Liaw:** Investigation, Methodology, Funding acquisition, Writing - review & editing, Project administration, Resources, Supervision.

Acknowledgements

The authors would like to deeply appreciate the supports from the Foundation for Innovative Research Groups of the National Natural Science Foundation of China (Grant No. 51621004), the National Natural Science Foundation of China (51871092, 11772122, 51625404, 51771232, and 51671217), the State Key Laboratory of Advanced Design and Manufacturing for Vehicle Body (71865015), State Key Laboratory of Powder Metallurgy, and the National Key Research and Development Program of China (2016YFB0700300 and 2016YFB1100103). The research is supported by Hunan Provincial Innovation Foundation For Postgraduate (CX2018B156). PKL very much appreciates the support of the U.S. Army Research Office Project (W911NF-13-1-0438 and W911NF-19-2-0049) with the program managers, Drs. M. P. Bakas, S. N. Mathaudhu, and D. M. Stepp. PKL thanks the support from the National Science Foundation (DMR-1611180 and 1809640) with the program directors, Drs. G. Shiflet and D. Farkas.

Appendix B. Supplementary data

Supplementary data to this article can be found online at https://doi.org/10.1016/j.intermet.2020.106741.

Appendix A

In this appendix, details of separate strengthening in Eq. (1) are introduced. Based on the Kocks-Mecking model [56–58], the dislocation density in the grain interior can be written as

$$\frac{\partial\rho}{\partial\varepsilon^P}=M\left(k+k_1\sqrt{\rho}-k_2\rho-k_e\rho\right) \tag{A.1}$$

where $k=k_3/(bd_G)$, $k_1=\psi/b$, and $k_2=k_{20}(\dot{\varepsilon}^p/\dot{\varepsilon}_0)^{-1/m}$, k_3 is a geometric factor dependent on the grain shape and dislocations arriving at GBs, d_G is the grain size, b is the magnitude of the Burgers vector, ψ is a proportionality factor, k_{20} is the dynamic recovery constant, $\dot{\varepsilon}_0$ is the reference strain rate, m is inversely proportional to the temperature, and k_e is an additional dynamic recovery factor based on the previous work [41]. The first two terms on the right-hand side of Eq. (A.1) represent the athermal storage of dislocations, the third term denotes the annihilation of dislocations during the dynamic recovery, which is independent of grain size, and the last term is related to the excess dislocation dynamic recovery introduced by nanoscale grains. k_e can be written as

$$k_e=(d_e/d_G)^2 \tag{A.2}$$

where d_e is the critical grain size that symbolizes the occurrence of the reinforced dynamic recovery.

The GB strengthening can be expressed by the Hall-Petch relationship as

$$\sigma_{GB}=k_{HP}/{d_G}^{1/2} \tag{A.3}$$

where k_{HP} is the Hall-Petch constant of alloys.

The solid-solution strengthening, σ_{ss}, denotes the contribution to the flow stress arising from the solutes in nanocrystalline HEAs. The solid-solution strengthening introduced by a single element in HEAs is calculated based on Eq. (2). The mismatch parameter, δ_i, in Eq. (2) can be expressed as [59].

$$\delta_i=\xi\left(\delta G_i^2+\beta^2\delta r_i^2\right)^{1/2} \tag{A.4}$$

where ξ is equal to 1. It is generally believed that $3<\beta<16$ for screw dislocations, and $\beta>16$ for edge dislocations [44,45]. Here, β is equal to 16 due to that the dominant dislocations are of an edge type in HEAs. The elastic mismatch, δG_i, and the atomic size mismatch, δr_i, introduced by the element, i, can be expressed as follows:

$$\delta r_i=\frac{\delta r_{ijklm}^{ave}-\delta r_{jklm}^{ave}}{\delta c_i} \tag{A.5}$$

$$\delta G_i=\frac{\delta G_{ijklm}^{ave}-\delta G_{jklm}^{ave}}{\delta c_i} \tag{A.6}$$

where δr_{ijklm}^{ave} and δG_{ijklm}^{ave} denote the average atomic-size mismatch and the average elastic mismatch of the *ijklm* HEA. δr_{jklm}^{ave} and δG_{jklm}^{ave} represent the average atomic-size mismatch and the average elastic mismatch of the *jklm* HEA. δc_i represents the atomic fraction difference of the element, i, between the *ijklm* and *jklm* HEAs. The average elastic mismatch and atomic-size mismatch of HEAs in Eqs. (A.5) and (A.6) can be expressed as

$$\delta r^{ave} = \sum_{i}^{n} \sum_{j}^{n} c_i c_j \delta r_{ij} = (c_1, c_2, \cdots, c_n) \begin{pmatrix} \delta r_{11} & \delta r_{12} & \cdots & \delta r_{1n} \\ \delta r_{21} & \delta r_{22} & \cdots & \delta r_{2n} \\ \vdots & \cdots & \ddots & \vdots \\ \delta r_{n1} & \delta r_{n2} & \cdots & \delta r_{nn} \end{pmatrix} \begin{pmatrix} c_1 \\ c_2 \\ \vdots \\ c_n \end{pmatrix} \tag{A.7}$$

$$\delta G^{ave} = \sum_{i}^{n} \sum_{j}^{n} c_i c_j \delta G_{ij} = (c_1, c_2, \cdots, c_n) \begin{pmatrix} \delta G_{11} & \delta G_{12} & \cdots & \delta G_{1n} \\ \delta G_{21} & \delta G_{22} & \cdots & \delta G_{2n} \\ \vdots & \cdots & \ddots & \vdots \\ \delta G_{n1} & \delta G_{n2} & \cdots & \delta G_{nn} \end{pmatrix} \begin{pmatrix} c_1 \\ c_2 \\ \vdots \\ c_n \end{pmatrix} \tag{A.8}$$

where δG_{ij} and δr_{ij} denote the elastic mismatch and the atomic-size mismatch between the atoms, i and j, which can be written as [45].

$$\delta r_{ij} = 2\left(r_i - r_j\right) / \left(r_i + r_j\right) \tag{A.9}$$

$$\delta G_{ij} = 2\left(G_i - G_j\right) / \left(G_i + G_j\right) \tag{A.10}$$

where r_i and r_j are the atomic radii, G_i and G_j are the shear moduli of pure metal crystals i and j, respectively. Lastly, the solid-solution strengthening in the HEA can be expressed based on Eq. (2).

The back stress, σ_b, is originating from the accumulation of dislocations at GBs [60], which can be expressed as

$$\sigma_b = M \frac{\mu b}{d_G} N \tag{A.11}$$

where N is the number of dislocations accumulating at GBs of the nanograined metal, which is determined by the following plastic-strain evolution law

$$\frac{dN}{d\varepsilon^P} = \frac{\zeta}{b}\left(1 - \frac{N}{N_B}\right) \tag{A.12}$$

where ε^P is the plastic strain, ζ and N_B are the mean distances between slip bands and the maximum numbers of dislocation loops at the GBs, respectively. The corresponding parameters used is listed in Table 3.

References

[1] J.W. Yeh, S.K. Chen, S.J. Lin, J.Y. Gan, T.S. Chin, T.T. Shun, C.H. Tsau, S.Y. Chang, Nanostructured high-entropy alloys with multiple principal elements: novel alloy design concepts and outcomes, Adv. Eng. Mater. 6 (2004) 299–303.

[2] B. Cantor, I.T.H. Chang, P. Knight, A.J.B. Vincent, Microstructural development in equiatomic multicomponent alloys, Mater. Sci. Eng., A 375–377 (2004) 213–218.

[3] Y. Zhang, T.T. Zuo, Z. Tang, M.C. Gao, K.A. Dahmen, P.K. Liaw, Z.P. Lu, Microstructures and properties of high-entropy alloys, Prog. Mater. Sci. 61 (2014) 1–93.

[4] Y. Yao, Z. Huang, P. Xie, S.D. Lacey, R.J. Jacob, H. Xie, D. Yu, Carbothermal shock synthesis of high-entropy-alloy nanoparticles, Science 359 (2018) 1489–1494.

[5] O. El-Atwani, N. Li, M. Li, A. Devaraj, J.K.S. Baldwin, M.M. Schneider, E. Martinez, Outstanding radiation resistance of tungsten-based high-entropy alloys, Sci. Adv. 5 (2019) 2002.

[6] E.P. George, D. Raabe, R.O. Ritchie, High-entropy alloys, Nat. Rev. Mater. 4 (2019) 515–534.

[7] C. Niu, C.R. LaRosa, J. Miao, M.J. Mills, M. Ghazisaeidi, Magnetically-driven phase transformation strengthening in high entropy alloys, Nat. Commun. 9 (2018) 1363.

[8] Z. Lei, X. Liu, Y. Wu, H. Wang, S. Jiang, S. Wang, D. Raabe, Enhanced strength and ductility in a high-entropy alloy via ordered oxygen complexes, Nature 563 (2018) 546.

[9] Y.J. Liang, L. Wang, Y. Wen, B. Cheng, Q. Wu, T. Cao, Y. Ren, High-content ductile coherent nanoprecipitates achieve ultrastrong high-entropy alloys, Nat. Commun. 9 (2018) 4063.

[10] A. Sarkar, Q. Wang, A. Schiele, M.R. Chellali, S.S. Bhattacharya, D. Wang, B. Breitung, High-entropy oxides: fundamental aspects and electrochemical properties, Adv. Mater. 31 (2019), 1806236.

[11] J. Liu, X. Guo, Q. Lin, Z. He, X. An, L. Li, P.K. Liaw, X.Z. Liao, L.P. Yu, J.P. Lin, L. Xie, J.L. Ren, Y. Zhang, Excellent ductility and serration feature of metastable CoCrFeNi high-entropy alloy at extremely low temperatures, Sci. China Mater. 62 (2019) 853–863.

[12] Z. Li, S. Zhao, R.O. Ritchie, M.A. Meyers, Mechanical properties of high-entropy alloys with emphasis on face-centered cubic alloys, Prog. Mater. Sci. 102 (2019) 296–345.

[13] S. Praveen, H.S. Kim, High-entropy alloys: potential candidates for high-temperature applications-an overview, Adv. Eng. Mater. 20 (2018), 1700645.

[14] Y. Zou, H. Ma, R. Spolenak, Ultrastrong ductile and stable high-entropy alloys at small scales, Nat. Commun. 6 (2015) 7748.

[15] F. Otto, A. Dlouhý, C. Somsen, H. Bei, G. Eggeler, E.P. George, The influences of temperature and microstructure on the tensile properties of a CoCrFeMnNi high-entropy alloy, Acta Mater. 61 (2013) 5743–5755.

[16] B. Gludovatz, A. Hohenwarter, D. Catoor, E.H. Chang, E.P. George, R.O. Ritchie, A fracture-resistant high-entropy alloy for cryogenic applications, Science 345 (2014) 1153–1158.

[17] Z. Fu, W. Chen, H. Wen, D. Zhang, Z. Chen, B. Zheng, E.J. Lavernia, Microstructure and strengthening mechanisms in an FCC structured single-phase nanocrystalline Co25Ni25Fe25Al7.5Cu17.5 high-entropy alloy, Acta Mater. 107 (2016) 59.

[18] J. Li, Q.H. Fang, B. Liu, Y. Liu, Y.W. Liu, Mechanical behaviors of AlCrFeCuNi high-entropy alloys under uniaxial tension via molecular dynamics simulation, RSC Adv. 6 (2016) 76409–76419.

[19] Z. Wang, J. Li, Q. Fang, B. Liu, L. Zhang, Investigation into nanoscratching mechanical response of AlCrCuFeNi high-entropy alloys using atomic simulations, Appl. Surf. Sci. 416 (2017) 470–481.

[20] Y. Afkham, M. Bahramyan, R.T. Mousavian, D. Brabazon, Tensile properties of AlCrCoFeCuNi glassy alloys: a molecular dynamics simulation study, Mater. Sci. Eng., A 698 (2017) 143–151.

[21] M. Bahramyan, R.T. Mousavian, D. Brabazon, Determination of atomic-scale structure and compressive behavior of solidified AlxCrCoFeCuNi high entropy alloys, Int. J. Mech. Sci. 171 (2019), 105389.

[22] J. Li, H. Chen, S. Li, Q.H. Fang, Y. Liu, L. Liang, H. Wu, P.K. Liaw, Tuning the mechanical behavior of high-entropy alloys via controlling cooling rates, Mater. Sci. Eng., A 760 (2019) 359–365.

[23] D. Utt, A. Stukowski, K. Albe, Grain boundary structure and mobility in high-entropy alloys: a comparative molecular dynamics study on a Σ11 symmetrical tilt grain boundary in face-centered cubic CuNiCoFe, Acta Mater. 186 (2020) 11–19.

[24] M. Bahramyan, R.T. Mousavian, D. Brabazon, Study of the plastic deformation mechanism of TRIP-TWIP high entropy alloys at the atomic level, Int. J. Plast. 127 (2020), 102649.

[25] Q. Fang, Y. Chen, J. Li, C. Jiang, B. Liu, Y. Liu, P.K. Liaw, Probing the phase transformation and dislocation evolution in dual-phase high-entropy alloys, Int. J. Plast. 114 (2019) 161–173.

[26] J. Li, Q. Fang, B. Liu, Y. Liu, Transformation induced softening and plasticity in high entropy alloys, Acta Mater. 147 (2018) 35–41.

[27] D. Choudhuri, B. Gwalani, S. Gorsse, M. Komarasamy, S.A. Mantri, S.G. Srinivasan, R. Banerjee, Enhancing strength and strain hardenability via deformation twinning in fcc-based high entropy alloys reinforced with intermetallic compounds, Acta Mater. 165 (2019) 420–430.

[28] J.F. Panzarino, Z. Pan, T.J. Rupert, Plasticity-induced restructuring of a nanocrystalline grain boundary network, Acta Mater. 120 (2016) 1–13.

[29] A. Prakash, D. Weygand, E. Bitzek, Influence of grain boundary structure and topology on the plastic deformation of nanocrystalline aluminum as studied by atomistic simulations, Int. J. Plast. 97 (2017) 107–125.

[30] S. Plimpton, Fast parallel algorithms for short-range molecular dynamics, Comput. Phys. 117 (1995) 1.

[31] X.W. Zhou, H.N.G. Wadley, R.A. Johnson, D.J. Larson, N. Tabat, A. Cerezo, T. F. Kelly, Atomic scale structure of sputtered metal multilayers, Acta Mater. 49 (2001) 4005–4015.

[32] A. Stukowski, Visualization and analysis of atomistic simulation data with OVITO-the Open Visualization Tool, Model. Simulat. Mater. Sci. Eng. 18 (2009), 015012.

[33] J.D. Honeycutt, H.C. Andersen, Molecular dynamics study of melting and freezing of small Lennard-Jones clusters, J. Phys. Chem. 91 (1987) 4950–4963.

[34] S. Liu, Y. Wei, The Gaussian distribution of lattice size and atomic level heterogeneity in high entropy alloys, Ext. Mech. Lett. 11 (2017) 84–88.

[35] A.J. Zaddach, C. Niu, C.C. Koch, D.L. Irving, Mechanical properties and stacking fault energies of NiFeCrCoMn high-entropy alloy, J. Occup. Med. 65 (2013) 1780–1789.

[36] S.K.R. Patil, S.V. Khare, B.R. Tuttle, J.K. Bording, S. Kodambaka, Mechanical stability of possible structures of PtN investigated using first-principles calculations, Phys. Rev. B 73 (2006), 104118.

[37] D. Iotova, N. Kioussis, S.P. Lim, Electronic structure and elastic properties of the Ni3X (X=Mn, Al, Ga, Si, Ge) intermetallics, Phys. Rev. B 54 (1996) 14413.

[38] Y.T. Zhu, X.Z. Liao, X.L. Wu, Deformation twinning in nanocrystalline materials, Prog. Mater. Sci. 57 (2012) 1–62.

[39] G.R. Cowper, P.S. Symonds, Strain-hardening and Strain-Rate Effects in the Impact Loading of Cantilever Beams, Division of Applied Mathematics, Brown University, Providence, Rhode Island, 1957.

[40] L. Zhu, H. Ruan, X. Li, M. Dao, H. Gao, J. Lu, Modeling grain size dependent optimal twin spacing for achieving ultimate high strength and related high ductility in nanotwinned metals, Acta Mater. 59 (2011) 5544–5557.

[41] J. Li, A.K. Soh, Modeling of the plastic deformation of nanostructured materials with grain size gradient, Int. J. Plast. 39 (2012) 88–102.

[42] J. Li, W. Lu, S. Chen, C. Liu, Revealing extra strengthening and strain hardening in heterogeneous two-phase nanostructures, Int. J. Plast. 126 (2020), 102626.

[43] F. Tan, Q. Fang, J. Li, H. Feng, Enhanced nanotwinning by special grain growth in nanocrystalline materials, J. Mater. Sci. 55 (2020) 3618–3628.

[44] C. Lee, G. Song, M.C. Gao, R. Feng, P. Chen, J. Brechtl, Y. Chen, K. An, W. Guo, J. D. Poplawsky, S. Li, A.T. Samaei, W. Chen, A. Hu, H. Choo, P.K. Liaw, Lattice distortion in a strong and ductile refractory high-entropy alloy, Acta Mater. 160 (2018) 158–172.

[45] O.N. Senkov, J.M. Scott, S.V. Senkova, D.B. Miracle, C.F. Woodward, Microstructure and room temperature properties of a high-entropy TaNbHfZrTi alloy, J. Alloys Compd. 509 (2011) 6043–6048.

[46] A.R. Denton, N.W. Ashcroft, Vegard's law, Phys. Rev. 43 (1991) 3161–3164.

[47] H. Ghaffarian, A.K. Taheri, K. Kang, S. Ryu, Molecular dynamics simulation study of the effect of temperature and grain size on the deformation behavior of polycrystalline cementite, Scripta Mater. 95 (2015) 23–26.

[48] Q. Ding, Y. Zhang, X. Chen, X. Fu, D. Chen, S. Chen, M. Wen, T. Zhu, R.O. Ritchie, Q. Yu, Tuning element distribution, structure and properties by composition in high-entropy alloys, Nature 574 (2019) 223–227.

[49] R.R. Eleti, T. Bhattacharjee, A. Shibata, N. Tsuji, Unique deformation behavior and microstructure evolution in high temperature processing of HfNbTaTiZr refractory high entropy alloy, Acta Mater. 171 (2019) 132–145.

[50] D.H. Lee, I.C. Choi, G. Yang, Z. Lu, M. Kawasaki, U. Ramamurty, J.I. Jang, Activation energy for plastic flow in nanocrystalline CoCrFeMnNi high-entropy alloy: a high temperature nanoindentation study, Scripta Mater. 156 (2018) 129–133.

[51] D. Guo, S. Song, R. Luo, W.A. Goddard III, M. Chen, K.M. Reddy, Q. An, Grain boundary sliding and amorphization are responsible for the reverse Hall-Petch relation in superhard nanocrystalline boron carbide, Phys. Rev. Lett. 121 (2018), 145504.

[52] W.F. Hosford, Mechanical Behavior of Materials, Cambridge University Press, New York, 2005.

[53] M. Dupraz, Z. Sun, C. Brandl, H. Van Swygenhoven, Dislocation interactions at reduced strain rates in atomistic simulations of nanocrystalline Al, Acta Mater. 144 (2018) 68–79.

[54] H. Van Swygenhoven, J.R. Weertman, Deformation in nanocrystalline metals, Mater. Today 9 (2006) 24–31.

[55] A. Leach, Molecular Modelling: Principles and Applications, second ed., Prentice Hall, Dorset, England, 2001.

[56] H. Mecking, U.F. Kocks, Kinetics of flow and strain-hardening, Acta Metall. 29 (1981) 1865–1875.

[57] L. Capolungo, C. Jochum, M. Cherkaoui, J. Qu, Homogenization method for strength and inelastic behavior of nanocrystalline materials, Int. J. Plast. 21 (2005) 67–82.

[58] L. Capolungo, M. Cherkaoui, J. Qu, On the elastic-viscoplastic behavior of nanocrystalline materials, Int. J. Plast. 23 (2007) 561–591.

[59] R. Labusch, A statistical theory of solid solution hardening, Phys. Status Solidi 41 (1970) 659.

[60] C.W. Sinclair, W.J. Poole, Y. Bréchet, A model for the grain size dependent work hardening of copper, Scripta Mater. 55 (2006) 739–742.